Journal of Power Sources 183 (2008) 799–804

Contents lists available at ScienceDirect

Journal of Power Sources

journal homepage: www.elsevier.com/locate/jpowsour

Electrochemical oxidation behavior of Mg–Li–Al–Ce–Zn and Mg–Li–Al–Ce–Zn–Mn in sodium chloride solution

Dianxue Cao*, Lin Wu, Guiling Wang, Yanzhuo Lv

Key Laboratory of Superlight Material and Surface Technology of Ministry of Education, Harbin Engineering University, Harbin 150001, PR China

ARTICLE INFO

Article history:
Received 11 April 2008
Received in revised form 2 June 2008
Accepted 4 June 2008
Available online 8 June 2008

Keywords:
Mg–Li–Al–Ce–Zn
Mg–Li–Al–Ce–Zn–Mn
Electrochemical oxidation
Utilization efficiency
Magnesium–hydrogen peroxide semi-fuel cell

ABSTRACT

Mg–Li–Al–Ce–Zn and Mg–Li–Al–Ce–Zn–Mn alloys were prepared using a vacuum induction melting method. Their electrochemical oxidation behavior in 0.7 M NaCl solution was investigated by means of potentiodynamic polarization, potentiostatic oxidation, electrochemical impedance technique and scanning electron microscopy examination. Their utilization efficiencies and performances as anode of metal–hydrogen peroxide semi-fuel cell were determined. The Mg–Li–Al–Ce–Zn–Mn exhibited higher discharge activity and utilization efficiency than Mg–Li–Al–Ce–Zn, and gave improved fuel cell performance. The utilization efficiency of Mg–Li–Al–Ce–Zn–Mn is comparable with that of the state-of-the-art magnesium alloy anode AP65. The magnesium–hydrogen peroxide semi-fuel cell with Mg–Li–Al–Ce–Zn–Mn anode presented a maximum power density of 91 mW cm^{-2} at room temperature. Scanning electron microscopy and electrochemical impedance studies indicated that the alloying element Mn prevented the formation of dense oxide film on the alloy surface and facilitated peeling off of the oxidation products.

1. Introduction

Magnesium–hydrogen peroxide semi-fuel cell has been developed as power source for low rate, long endurance unmanned undersea vehicle (UUV) [1,2]. This electrochemical system consists of a magnesium anode, a sodium chloride anolyte, a conductive membrane, a cathode catalyst, and a catholyte of sodium chloride, sulfuric acid and hydrogen peroxide. The theoretical half-cell and overall cell reactions as well as standard potentials for this system are as follows [2–5]:

$$Mg \rightarrow Mg^{2+} + 2e^{-}, \quad E^0 = 2.37\,V \text{ vs. SHE}$$

$$H_2O_2 + 2H^+ + 2e^- \rightarrow 2H_2O, \quad E^0 = 1.77\,V \text{ vs. SHE}$$

$$Mg + H_2O_2 + 2H^+ \rightarrow Mg^{2+} + 2H_2O, \quad E^0_{cell} = 4.14\,V$$

Magnesium as anode has advantages of high Faradic capacity (2.2 Ah g^{-1}), high specific energy (6.8 kWh kg^{-1}) and more negative standard electroreduction potential (−2.37 V vs. standard hydrogen electrode (SHE)) [6]. Hydrogen peroxide as cathode oxidant in acid medium has advantages of fast electroreduction rate, more positive standard electroreduction potential (1.77 V vs. SHE) and easy handling, storage and feeding to a fuel cell due to its liquid form [7–10]. The combination of these advantages as well as using seawater as electrolyte make magnesium–hydrogen peroxide semi-fuel cell an attractive undersea power source because the system has high specific energy, stable discharging ability, short mechanically recharge time, long dry storage life, ability to work at ambient pressure, environmentally acceptability, reliability, safety and low cost [2].

Magnesium anode of Mg–H_2O_2 semi-fuel cells is either pure magnesium or magnesium alloys, such as AZ61 [2,11]. Medeiros et al. [2,3] investigated a Mg–H_2O_2 semi-fuel cell using magnesium alloy AZ61 as anode and carbon fiber supported Pd–Ir as cathode catalyst. They found that the cell has a voltage of above 1.7 V at 25 mA cm^{-2} at room temperature. The magnesium efficiency is around 80%. The specific energy of the system ranges from 500 to 520 Wh kg^{-1} based on the weights consumed during discharge of the magnesium anode, hydrogen peroxide and acid. Yang et al. [11] reported that using pure magnesium anode and Pd–Ag coated nickel foam cathode, the cell voltage is about 1.6 V at 25 mA cm^{-2} at room temperature.

Thermodynamically, magnesium anodes should exhibit very negative potentials. However, in practical, these electrodes operate at significantly less negative potentials because: (a) magnesium anodes are normally covered by passive oxide films which cause a delay in reaching a steady-state and reduce discharging rate; (b) magnesium anodes undergo parasitic corrosion reaction, or self-discharge, resulting in the reduction of Columbic efficiency (less than 100% utilization of the metal) and the evolution of hydrogen.

* Corresponding author. Tel.: +86 451 82589036; fax: +86 451 82589036.
E-mail address: caodianxue@hrbeu.edu.cn (D. Cao).

0378-7753/$ – see front matter © 2008 Elsevier B.V. All rights reserved.
doi:10.1016/j.jpowsour.2008.06.005

There are in general two ways to improve the magnesium anode performance. One is to dope the magnesium with other elements (known as "activation"). The second is to modify the electrolyte by including additives. Both methods can inhabit the formation and/or accelerate the elimination of oxide layers and suppress corrosive dissolution [12].

The improvement of magnesium anode performance by the addition of alloying elements to pure magnesium has not been well investigated [13,14]. Udhayan et al. [13] reported that magnesium alloy AP65 (Al: 6–7%, Pb: 4.5–5%, Zn: 0.14–1.5%, Mn: 0.15–1.3%) has a hydrogen evolution rate of 0.15 mL min^{-1} cm^{-2} and a utilization efficiency of 84.6%. The open circuit potential of this alloy measured in seawater is −1.803 V versus saturated calomel reference electrode (SCE). Sivashanmugam et al. [15] investigated Mg–Li alloy with 13 wt% Li for possible use in magnesium primary reserve batteries. They found that this Mg–Li alloy exhibits higher anodic efficiencies (81%) even when the current density is increased to 8.6 mA cm^{-2}. The Mg–Li/$MgCl_2$/CuO cells offer higher operating voltage and capacity than those with the conventionally used Mg–Al alloy. We recently reported that Mg–Li-based alloys, such as Mg–Li, Mg–Li–Al, and Mg–Li–Al–Ce, exhibited higher electrooxidation activity in NaCl solution than commercial magnesium alloy AZ3 [16]. The utilization efficiency of the quaternary Mg–Li–Al–Ce reached as high as around 82%. The discharge activities and utilization efficiencies of these alloys increase in the order: Mg–Li < Mg–Li–Al < Mg–Li–Al–Ce. The oxidation products of Mg–Li, Mg–Li–Al and Mg–Li–Al–Ce were loosely adhered to the alloys surfaces, which is partially responsible for the high discharge activity.

In this study, Mg–Li–Al–Ce–Zn and Mg–Li–Al–Ce–Zn–Mn alloys were prepared. Their discharge behavior in NaCl solution was studied. Mg–H_2O_2 semi-fuel cells using these alloys as anode were fabricated and their performances were evaluated. The purpose of this study is to investigate the effects of the alloying elements Zn and Mn on the electrochemical oxidation performance of Mg–Li–Al–Ce alloy and find better magnesium anodes for Mg–H_2O_2 semi-fuel cells and seawater batteries.

2. Experimental

2.1. Preparation of magnesium alloys

Mg–Li–Al–Ce–Zn and Mg–Li–Al–Ce–Zn–Mn alloys were prepared from ingots of pure magnesium (99.99%), pure lithium (99.99%), pure aluminum (99.99%), pure Zn (99.99%), pure Mn (99.99%) and Mg–Ce alloy containing 26.6 wt% Ce using a vacuum induction melting furnace. The induction furnace containing a refractory lined crucible surrounded by an induction coil is located inside a vacuum chamber. The induction furnace is connected to an AC power source at a frequency precisely matched to the furnace size and material being melted. Magnesium and the alloying components were charged into the induction furnace under the protection of ultrahigh purity Argon. The furnace was then evacuated to 1.0×10^{-2} Pa, and charged with ultrahigh purity argon. AC power was applied to melt the charge under flowing argon atmosphere. A preheated tundish-casting mold assembly was inserted through a valve, and the refractory tundish was positioned in front of the induction furnace. The molten metals were poured through the tundish into the awaiting stainless steel mold (Ø6 cm × 18 cm). The mold containing hot melts was cooled down to ambient temperature under argon atmosphere in the furnace within 2 h. The prepared alloys were used in the cast state. The nominal compositions of the alloys are given in Table 1.

The alloy ingots were machined to 20 mm × 20 mm × 2 mm to serve as the working electrode for electrochemical measurements.

Table 1
Nominal composition of the alloys (wt%)

Alloys	Mg	Li	Al	Zn	Ce	Mn
Mg–Li–Al–Zn–Ce	89.1	5	3.5	1.2	1.2	–
Mg–Li–Al–Zn–Ce–Mn	87.6	5	3.5	1.2	1.2	1.5

Prior to each experiment, the alloy surface facing to the electrolyte was mechanically polished with SiC abrasive paper down to 700 grit, degreased with acetone, washed with deoxygenated ultrapure water (Milli-Q), and then immediately assembled into the electrochemical cell.

2.2. Electrochemical measurements

A specifically designed home-made three-electrode electrochemical cell was used to carry out the electrochemical measurements of magnesium alloys [16]. The cell has a defined exposure area of the magnesium alloy working electrode, which is 0.95 cm^2. This area was used to calculate the current density. A blackened platinum wire mesh served as the auxiliary electrode. A saturated calomel reference electrode with the Luggin capillary positioned closing to the alloy surface was used as the reference electrode. Unless indicated otherwise, all potentials are referred to SCE (0.241 V vs. SHE). A VMP3/Z potentiostat (Princeton Applied Research) controlled by a computer with EC-lab software was used in the electrochemical measurements. All electrochemical experiments were performed at room temperature in 0.7 M NaCl aqueous solutions (purged with Ar before transferred into the cell), chosen in order to mimic seawater. All solutions were made with analytical grade chemical reagents and Millipore Milli-Q water (resistivity > 18 MΩ cm).

Potentiodynamic polarization curves were obtained by sweeping the potential from −2.2 to −0.4 V at a scan rate of 5 mV s^{-1} after the alloy samples were polarized at −2.2 V for 5 min. Potentiostatic current–time curves were measured by holding the working electrode (alloy specimen) for 10 min at each constant potential of −1.4, −1.2, −1.0 and −0.8 V. Electrochemical impedance spectra were recorded at various potentials in the range of −1.4 to −0.8 V after the electrode was kept at the measuring potential for 10 min. The excitation voltage is 10 mV and the frequency varied from 20 kHz to 0.01 Hz. The surface morphologies of the alloy specimen were examined using scanning electron microscopy (SEM; JEOL JSM-6480). Images were acquired using a 20 kV accelerating voltage.

In order to measure the utilization efficiency of the magnesium alloys, the weighted alloy coupons were discharged by holding at constant potentials for certain time while recording the current–time curves. The reaction products remaining attached on the alloy surfaces after discharge were removed using a scratch blade and high-speed water spray. The cleaned remaining alloy coupons were then dried and weighed. The alloy utilization efficiency (η) was calculated using Eq. (1).

$$\eta(\%) = \frac{(Q/nF)M_a}{W_i - W_f} \times 100 \quad (1)$$

where Q is the charge in Coulomb obtained by the integration of current–time curve, F is Faraday constant (96,485 C mol^{-1}), W_i and W_f are the weight of alloy samples in gram before and after discharge, respectively, n is the average number of electron per discharge reaction assuming the oxidation states of the products are 2+ for Mg, Zn and Mn, 1+ for Li, 3+ for Al and Ce. M_a is the average atomic mass (g mol^{-1}) of the sample. n and M_a were calculated by

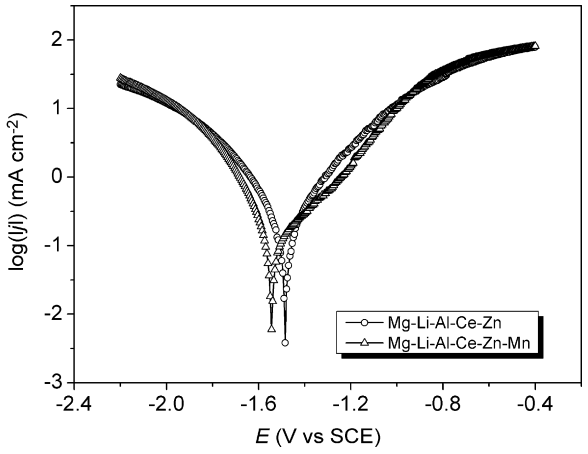

Fig. 1. Potentiodynamic polarization curves for Mg–Li–Al–Ce–Zn and Mg–Li–Al–Ce–Zn–Mn measured in 0.7 M NaCl solution at a scan rate of 5 mV s^{-1}.

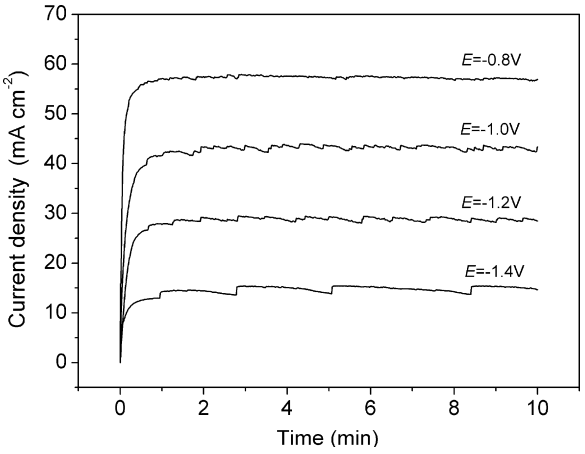

Fig. 2. Current–time curves for Mg–Li–Al–Ce–Zn recorded in 0.7 M NaCl solution at various anodic potentials.

Eqs. (2) and (3), respectively.

$$n = \sum x_i z_i \quad (2)$$

$$M_a = \sum x_i M_i \quad (3)$$

where x_i is the mole fraction, z_i is the oxidation state, and M_i is the atomic mass of component i.

2.3. Mg–H_2O_2 semi-fuel cell tests

The performance of magnesium alloys as anode of Mg–H_2O_2 semi-fuel cell was examined using a home-made flow through test cell made of Plexiglas. The geometrical area of the anode (Mg alloys) and the cathode (Ir/Pd coated nickel foam) was 4.0 cm^2 (20 mm × 20 mm). Nafion-115 (DuPont) membrane was used to separate the anode and the cathode compartments. The anolyte (0.7 M NaCl) and the catholyte (0.7 M NaCl + 0.1 M H_2SO_4 + 0.5 M H_2O_2) were pumped into the bottom of the anode and the cathode compartments, respectively, and exited at the top of the compartments. The flow rate is 100 mL min^{-1} for both the anolyte and the catholyte and is controlled by individual peristaltic pump. The performance of the Mg–H_2O_2 was recorded at ambient temperature using a computer-controlled E-load system (Arbin).

3. Results and discussion

3.1. Potentiodynamic polarization

Fig. 1 shows the potentiodynamic polarization curves of Mg–Li–Al–Ce–Zn and Mg–Li–Al–Ce–Zn–Mn measured in 0.7 M NaCl solution (1st sweep in the positive-going direction). The curves were taken after the electrodes were cathodically polarized at −2.2 V for 5 min. It can be seen that the corrosion potential of Mg–Li–Al–Ce–Zn–Mn (−1.54 V) is slightly more negative than that of Mg–Li–Al–Ce–Zn (−1.48 V), which might be associated to the difference in chemical composition and structure of the magnesium alloys.

3.2. Potentiostatic oxidations

The current–time curves measured at various anodic potentials in 0.7 M NaCl for Mg–Li–Al–Ce–Zn and Mg–Li–Al–Ce–Zn–Mn are shown in Figs. 2 and 3, respectively. The current–time profiles are similar for both samples, i.e. the anodic current increased rapidly in the early discharging stage and then reached to an approximate constant value. The discharge currents increased with the increase of polarization potential from −1.4 to −0.8 V for both samples. The stabilized discharge current density of Mg–Li–Al–Ce–Zn–Mn is around 5 mA cm^{-2} higher than that of Mg–Li–Al–Ce–Zn under the same discharge potentials. Mg–Li–Al–Ce–Zn displays a similar anodic current density with Mg–Li–Al–Ce (e.g. 44 mA cm^{-2} at −1.0 V as we previously reported) [16]. These results demonstrated that Mg–Li–Al–Ce–Zn–Mn has higher discharge activity than Mg–Li–Al–Ce–Zn, Mg–Li–Al–Ce and commercial magnesium alloy AZ31 (32 mA cm^{-2} at −1.0 V) [16]. The discharge current densities of our magnesium alloys are higher than aluminum alloys under the similar experimental conditions. For example, the current density of Al–In polarized at −1.05 V versus SCE for 20 min in 0.6 M NaCl are around 32 mA cm^{-2} [17].

Even though the overall discharge currents for both Mg–Li–Al–Ce–Zn and Mg–Li–Al–Ce–Zn–Mn alloys exhibit no sign of decrease within the test period at various potentials, the currents fluctuated periodically at anodic potentials lower than −1.0 V for Mg–Li–Al–Ce–Zn and −1.2 V for Mg–Li–Al–Ce–Zn–Mn. This behavior might be attributed to the formation, accumulation and shedding of oxidation products. The oxidation products, remaining attached on the alloy surface, blocked the alloy surface from contact with the electrolyte, leading to the decrease of active electrode area. When the oxides came off, the

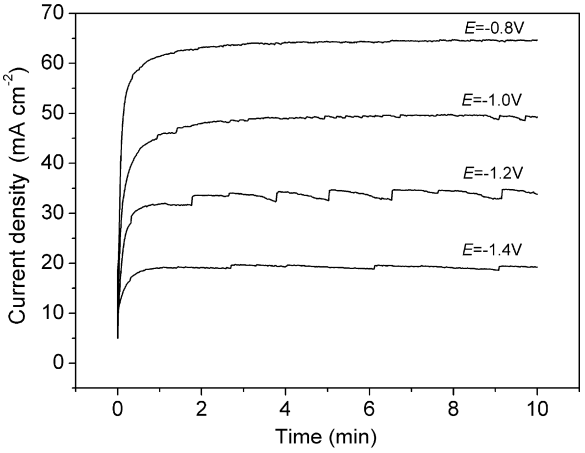

Fig. 3. Current–time curves for Mg–Li–Al–Ce–Zn–Mn recorded in 0.7 M NaCl solution at various anodic potentials.

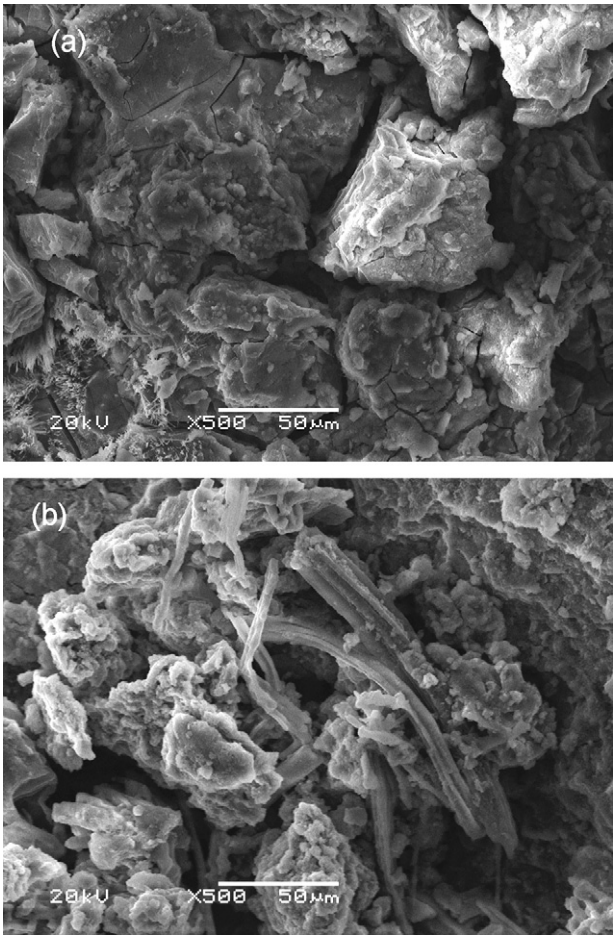

Fig. 4. SEM micrographs of Mg–Li–Al–Ce–Zn (a) and Mg–Li–Al–Ce–Zn–Mn (b).

electrode area was regenerated, and the discharge currents bounced back.

Fig. 4a and b shows the SEM micrographs of Mg–Li–Al–Ce–Zn and Mg–Li–Al–Ce–Zn–Mn, respectively. The images were taken after the samples were consecutively discharged at −1.4, −1.2, −1.0 and −0.8 V each for 10 min. Fig. 4a indicated that the oxidation products of Mg–Li–Al–Ce–Zn formed relatively large and dense micro-blocks on the surface. Fig. 4b demonstrated that the discharge products remaining attached on Mg–Li–Al–Ce–Zn–Mn surface present as loosely packed aggregates of micro-clumps and wires. Clearly, the morphologies of the oxidized surface of the two alloys are different. The loosely packed oxidation products of Mg–Li–Al–Ce–Zn–Mn, on one hand, allowed the electrolyte to penetrate through, on the other hand, they come off more easily. Consequently, Mg–Li–Al–Ce–Zn–Mn alloy retains larger reaction surface area than Mg–Li–Al–Ce–Zn during discharge, which might be responsible for the higher discharge current density of Mg–Li–Al–Ce–Zn–Mn. So SEM results suggested that alloying element of Mn prevented the formation of dense passive films and facilitated the film peeling off from alloy surfaces.

Electrochemical impedance technique was used to qualitatively compare the discharge behavior of the two magnesium alloy samples. Figs. 5 and 6 show the Nyquist plots of Mg–Li–Al–Ce–Zn and Mg–Li–Al–Ce–Zn–Mn, respectively. The impedance spectra recorded at open circuit potential (OPC) for both Mg–Li–Al–Ce–Zn and Mg–Li–Al–Ce–Zn–Mn are characterized by a single high frequency capacitive semicircle. The diameter of the semicircle, representing the polarization resistance R_p, for Mg–Li–Al–Ce–Zn and

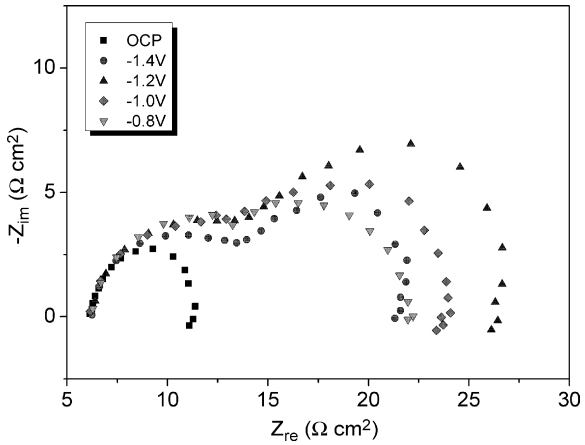

Fig. 5. Impedance spectra for Mg–Li–Al–Ce–Zn recorded at various anodic polarization potentials after discharging for 10 min at the measuring potentials in 0.7 M NaCl.

Mg–Li–Al–Ce–Zn–Mn is nearly the same (around 5.5 Ω cm^2). The impedance spectra measured at various applied anodic polarization potentials between −1.4 and −0.8 V for Mg–Li–Al–Ce–Zn–Mn are quite different from those for Mg–Li–Al–Ce–Zn. The Nyquist plot of Mg–Li–Al–Ce–Zn–Mn remains a single capacitive semicircle at anodic potentials, but the diameter of the semicircle depends on the anodic polarization potential (Fig. 5). The Nyquist plots of Mg–Li–Al–Ce–Zn display a high frequency and a middle frequency capacitive loop (Fig. 6). According to literatures about impedance studies on conventional magnesium alloys, such as AZ91 and AZ61 [18–21], the high frequency capacitive loop observed in the impedance spectra of Mg–Li–Al–Ce–Zn and Mg–Li–Al–Ce–Zn–Mn might result from both charge transfer and a surface oxide film, the middle frequency capacitive loop observed in the spectra of Mg–Li–Al–Ce–Zn might be attributed to relaxation of mass transport (probably Mg^+) in the growing solid oxide phase (an aggregating layer) on the alloy surface. No middle frequency capacitive loop for Mg–Li–Al–Ce–Zn–Mn is an indication of absence of thick and dense surface oxide layers. This result is consistent with that of SEM.

The potential dependence of the diameter of the semicircles is the same for both Mg–Li–Al–Ce–Zn and Mg–Li–Al–Ce–Zn–Mn, that is, the diameters get larger with the increase of anodic polarization potential up to −1.2 V, and then get smaller with the

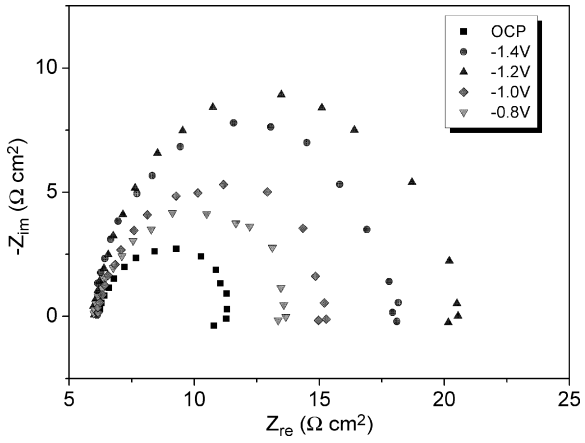

Fig. 6. Impedance spectra for Mg–Li–Al–Ce–Zn–Mn recorded at various anodic polarization potentials after discharging for 10 min at the measuring potentials in 0.7 M NaCl.

Table 2
Utilization efficiencies of magnesium alloys discharged in 0.7 M NaCl

	Utilization efficiency η (%)	
	Discharge at −1.2 V for 60 min	Discharge at −0.8 V for 30 min
Mg–Li–Al–Zn–Ce	78.8	82.2
Mg–Li–Al–Zn–Ce–Mn	82.1	85.6

further increase of potential up to −0.8 V. Similar behavior has been reported for commercial magnesium alloys such as AZ91 and AZ61 [18]. Since the charge transfer resistances are much smaller than the film resistance at the anodic polarization potentials [18,19], the change of the diameter with the anodic potential fairly reflected the change of oxide films formed on the alloy surface during discharge at different potentials. Based on this analysis, the potential dependence of the capacitive loop might suggest that, when the alloys were discharged at low anodic potential such as −1.2 V, the oxide film is likely more dense, homogeneous and protective, and when the alloys were discharged at high anodic potential, such as −0.8 V, the oxide film become less homogeneous and less dense. This is understandable because the fast discharge at high anodic potentials led to the break down and shedding of the oxide layers.

The utilization efficiencies of Mg–Li–Al–Ce–Zn and Mg–Li–Al–Ce–Zn–Mn were measured using a weight loss method. The measurements were carried out after discharging the samples at −1.2 V for 60 min and −0.8 V for 30 min, respectively. The utilization efficiency is defined as the ratio of the mass loss responsible for the generation of discharge current to the total mass loss within the discharge period. The results are given in Table 2. It can be seen that the utilization efficiency of Mg–Li–Al–Ce–Zn–Mn is around 3% higher than that of Mg–Li–Al–Ce–Zn at both discharge potentials, demonstrating that the alloying element of Mn played a role in enhancing the utilization efficiency of the alloy. The addition of Mn likely leads to a reduction of crystal grain size, which results in an increase of hydrogen evolution overpotential and a decrease of self-discharge rate, and consequently improved the discharge efficiency. The utilization efficiency of Mg–Li–Al–Ce–Zn–Mn reached as high as around 82–86%, which is close to that of the state-of-the-art magnesium alloy anode AP65 (84.7%) [13]. When the alloys were discharged at more positive anodic potential, the utilization efficiency gets higher. This is probably because that the hydrogen evolution and self-discharge rates were depressed at fast discharge rate.

3.3. Fuel cell performance

In order to evaluate the performance of Mg–Li–Al–Ce–Zn and Mg–Li–Al–Ce–Zn–Mn as the anode of metal–hydrogen peroxide semi-fuel cell, Mg–H_2O_2 semi-fuel cells were assemble and tested at room temperature. Fig. 7 demonstrates the cell voltage and power density versus current density plots. It can be seen that Mg–Li–Al–Ce–Zn–Mn anode exhibited better performance than Mg–Li–Al–Ce–Zn anode, especially at lower current density. The voltage of the cell using Mg–Li–Al–Ce–Zn–Mn anode is around 150 mV higher than that with Mg–Li–Al–Ce–Zn anode at current density lower than 50 mA cm^{-2}. The peak power density of the semi-fuel cell with Mg–Li–Al–Ce–Zn–Mn anode reached 91 mW cm^{-2}, which is higher than that of Mg–Li–Al–Ce–Zn anode (81 mW cm^{-2}). The voltages of both cells decay nearly linearly with the increase of current density until reaching to the mass transport control region, demonstrating that the cell performance shows a strong dependence on the ohmic resistance of the cell. Overvoltages due to kinetic limitations cannot be seen as they are probably masked by IR drop.

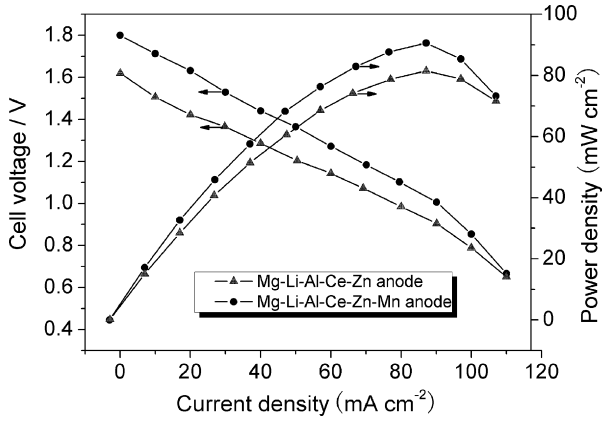

Fig. 7. Performance comparison of Mg–H_2O_2 semi-fuel cell with different anodes at room temperature. Anode: Mg–Li–Al–Ce–Zn and Mg–Li–Al–Ce–Zn–Mn. Cathode: Ir/Pd/Ni-foam. Anolyte: 0.7 M NaCl, 100 mL min^{-1}. Catholyte: 0.7 M NaCl + 0.5 MH_2O_2 + 0.1 M H_2SO_4, 100 mL min^{-1}.

4. Conclusions

Casting ingots of Mg–Li–Al–Ce–Zn and Mg–Li–Al–Ce–Zn–Mn alloys were prepared by induction smelting the pure metals with each other or with a Mg–Ce alloy under Ar atmosphere followed by surface grinding and cleaning. Their properties as potential anode material for metal semi-fuel cell and seawater battery were investigated. Both alloys demonstrated high discharge activity and utilization efficiency in NaCl solution. Mg–Li–Al–Ce–Zn–Mn gave better performance than Mg–Li–Al–Ce–Zn. The oxidation products of Mg–Li–Al–Ce–Zn–Mn formed less dense and less homogeneous surface layer, which is partially responsible for the high discharge activity. The utilization efficiency of the Mg–Li–Al–Ce–Zn–Mn alloy reached to more than 80% at typical discharge potentials. The magnesium–hydrogen peroxide semi-fuel cell using Mg–Li–Al–Ce–Zn–Mn anode displayed a maximum power density of 91 m W cm^{-2} at room temperature.

Acknowledgements

We gratefully acknowledge to Dr. Milin Zhang for assistance in alloy preparation. This work was financially supported by Key Laboratory of Superlight Material and Surface Technology of Ministry of Education and Harbin Engineering University (HEUFT07030).

References

[1] O. Hasvold, Power Sources 14 (1993) 243–255.
[2] M.G. Medeiros, R.R. Bessette, C.M. Deschenes, C.J. Patrissi, L.G. Carreiro, S.P. Tucker, D.W. Atwater, J. Power Sources 136 (2004) 226–231.
[3] M.G. Medeiros, R.R. Bessette, C.M. Deschenes, D.W. Atwater, J. Power Sources 96 (2001) 236–239.
[4] R.R. Bessette, M.G. Medeiros, C.J. Patrissi, C.M. Deschenes, C.N. LaFratta, J. Power Sources 96 (2001) 240–244.
[5] M.G. Medeiros, E.G. Dow, J. Power Sources 80 (1999) 78–82.
[6] R.P. Hamlen, D.W. Atwater, in: D. Linden, T.B. Reddy (Eds.), Handbook of Batteries, 3rd ed., McGraw-Hill, 2002, p. 381.
[7] R. O'Hayre, S.W. Cha, W. Colella, F.B. Prinz, Fuel Cell Fundamentals, Wiley, New York, 2006.
[8] N. Luo, G.H. Miley, P.J. Shrestha, R. Gimlin, R. Burton, G. Hawkins, J. Mather, J. Rusek, F. Holcomb, Proceedings of the Eighth International Hydrogen Peroxide Propulsion Conference, Purdue University, Lafayette, IN, USA, September 18–21, 2005, pp. 87–96.
[9] G.H. Miley, N. Luo, J. Mather, R. Burton, G. Hawkins, L. Gu, E. Byrd, R. Gimlin, P.J. Shrestha, G. Benavides, J. Laystrom, D. Carroll, J. Power Sources 165 (2007) 509–516.
[10] L. Gu, N. Luo, G.H. Miley, J. Power Sources 173 (2007) 77–85.
[11] W. Yang, S. Yang, W. Sun, G. Sun, Q. Xin, Electrochim. Acta 52 (2006) 9–14.
[12] Q. Li, N.J. Bjerrum, J. Power Sources 110 (2002) 1–10.
[13] R. Udhayan, N. Muniyandi, P.B. Mathur, Br. Corros. J. 27 (1992) 68–71.

[14] K.H. Oehr, S. Splinter, J.C.-Y. Jung, E.L. Gyenge, C.W. Oloman, US Patent 6,706,432 (2004).
[15] A. Sivashanmugam, T.P. kumar, N.G. Renganathan, S. Gopukumar1, J. Appl. Electrochem. 34 (2004) 1135–1139.
[16] D. Cao, L. Wu, Y. Sun, G. Wang, Y. Lv, J. Power Sources 177 (2008) 624–630.
[17] S.Z.E. Abedin, F. Endres, J. Appl. Electrochem. 34 (2004) 1071–1080.
[18] M. Anik, G. Celikten, Corros. Sci. 49 (2007) 1878–1894.
[19] F. Guadarrama-Munoz, J. Mendoza-Flores, R. Duran-Romero, J. Genesca, Electrochim. Acta 51 (2006) 1820–1830.
[20] G. Song, A. Atrens, X. Wu, B. Zhang, Corros. Sci. 40 (1998) 1769–1791.
[21] G. Baril, C. Blanc, N. Pebere, J. Electrochem. Soc. 148 (2001) B489–B496.